Progress In Electromagnetics Research, Vol. 118, 253–271, 2011

A COMPACT DUAL-POLARIZED BROADBAND ANTENNA WITH HYBRID BEAM-FORMING CAPABILITIES

H.-L. Peng[1,*], W.-Y. Yin[1,2], J.-F. Mao[1], D. Huo[3], X. Hang[3], and L. Zhou[1]

[1]Key Laboratory of Ministry of Education of China for Research of Design and Electromagnetic Compatibility of High Speed Electronic Systems, Shanghai Jiao Tong University, Shanghai 200240, China

[2]Center for Optical and EM Research, State Key Lab of MOI, Zhejiang University, Hangzhou 310058, China

[3]ZTE Corporation, Shanghai 201203, China

Abstract—A broadband dual-polarized four-port (DPFP) antenna is presented in this paper, which consists of a radiation element and a feed network. It is very compact in size, with the diameter of 150.0 mm and the height of 47.0 mm, with the following unique properties: (1) it has hybrid beam-forming capability and operates at two modes, which depends on its excitation; (2) its operating frequency range is from 0.96 to1.78 GHz, and the return loss is about 10 dB; (3) its insertion loss is (3 ± 0.5) dB, with its balanced power splitting over the relative bandwidths of 37% at Mode 1 ($180° \pm 5°$ phase shifting) and 55% at Mode 2 ($\pm 5°$ phase shifting), respectively; (4) an isolation of 30 dB at Mode 1 is obtained between the dual polarized ports, with the gain of 7.6 dBi and 42° of the 3 dB-bandwidth at 1.25 GHz; and (5) the gain difference between Modes 1 and 2 is about 7 dB, within the angle of $-15° \leq \theta \leq 15°$ for the same polarization at 1.25 GHz. For the application of DPFP, a hybrid beam forming algorithm is proposed with an angular precision of 7° and is validated by measurement.

1. INTRODUCTION

It is well known that various wireless communication systems [1] require many small antennas with broad impedance bandwidth,

Received 29 April 2011, Accepted 24 June 2011, Scheduled 5 July 2011

* Corresponding author: Hong-Li Peng (hl.peng@sjtu.edu.cn).

high isolation between orthogonal linear polarized signals, non-center feeding structures and fast beam-forming function. However, it is difficult for conventional planar antennas to meet these requirements, such as a center-fed spiral antenna [2], planar inverted-F antenna PIFA [3] and a single-fed microstrip antenna [4, 5], etc. On the other hand, multiple antennas [6, 7] and their based beamforming [8–11] also can not be used in this systems because of their un-acceptable large array size reasons.

To the best of our knowledge, in order to meet the above requirements, multi-port antennas have been proposed recently in [12], where different excitation and termination states are introduced. Further, these multi-port loading antennas were presented in [13–16], respectively, with miniaturized geometries, broadband and reconfigurable radiation pattern capabilities obtained. However, due to limited small physical space, there are two remaining challenges with the multi-port antennas, i.e., fast narrow beam forming and port isolation for multi-port antenna designs and realizations.

In this paper, we propose a compact broadband dual-polarized four-port (DPFP) antenna. The antenna is capable of achieving high port isolation and fast narrow beam which results to its target tracking capability with accuracy of 7°. By "tracking" we mean the ability of the antenna to detect the target moving into the perimeter of a cone that has the apex at the center of the antenna aperture. The DPFP antenna operates over the frequency range from 0.96–1.78 GHz and has at least 30 dB isolation between the dual linearly polarized ports. To achieve the design target, a hybrid fast beam forming approach is employed by combining both the switched RF sum-difference beam and digital beam forming. To enable this approach, a switched dual-mode RF feeding network is added at the receiver front-end and a DSP module is introduced to digital processing, together with a digital base band (DBB) first- and second-order beam forming schemes. The resulting DPFP antenna is a structure consisting of a radiation element and a feeding network. While computer simulation is deployed during the design using an EM software, a prototype is fabricated and measured in chamber to validate the designated radiation characteristics.

The paper is organized as following: Section 2 gives a detailed physical description of the DPFP antenna and Section 3 introduces the beam forming algorithm used, together with the calibration technique necessary to for the deployment of beam forming. Section 4 contains the simulated radiation characteristics of the DPFP antenna and the measurement results that verify the target detection accuracy. Final conclusions are left Section 5.

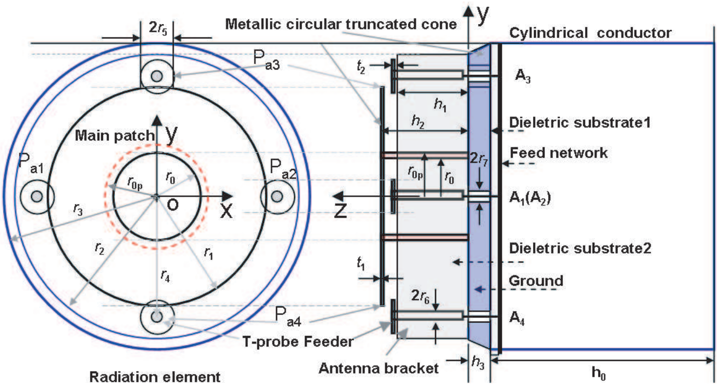

(a) (b)

Figure 1. Geometry of the compact four-port DPFP antenna located on a cylindrical conductor. (a) Top and (b) side views.

2. DESIGN METHOD FOR THE DPFP ANTENNA

Located on the surface of a cylindrical conductor, our DPFP antenna is made of two visible sub-structures i.e., a radiation element and a dual-mode feed network, as their structures shown in Figure 1.

2.1. Radiation Element

The radiation element consists of a patch, four T-probe feeders and a circular truncated cone. The patch is a metallic ring of t_1 in thickness, with its inner and outer radii of r_0 and r_1, respectively. The patch at its central area is mechanically supported by a metallic cylinder box, where the box in height of h_1, with its inner and outer radii of r_0 and $r_{0\text{p}}$, is also served as the electrical RF ground and frequency tuning device for the patch, a function necessary to improve the symmetry of antenna radiation pattern. Each of the four T-probe feeders, as denoted by P_{a1}, P_{a2}, P_{a3} and P_{a4} in Figure 1, is made of a small copper cap connected with a vertical copper cylinder. The thickness and radius of the cap are t_2 and r_5, respectively, while the height and radius of the cylinder are h_1 and r_6. The truncated cone made of aluminum, with a top radius r_2, a bottom radius r_3, and a height h_3, is integrated with the cylindrical conductor of radius r_3 and height h_0.

Being used as the ground for the antenna, the cylindrical conductor has impact on the antenna performance, and therefore its size has to be taken into account during design. Table 1 summarizes the geometrical parameters of the structure.

Table 1. Some geometrical parameters of the DPFP antenna (Unit: mm).

Parameter	h_0	h_1	h_2	h_3	r_0	r_1	r_2	r_3
Value	34.8	29.2	34.8	10.0	16.0	46.1	55.0	75.0
Parameter	r_4	r_5	r_6	r_7	t_1	t_2	G	r_{0p}
Value	50.0	7.2	2.7	2.7	2.2	1.2	200.0	17.0

Here, the antenna bracket is a dielectric ring with the relative permittivity of 2.2. The inner radius of the ring is 41.5 mm and outer radius is r_2. The four holes, with a radius r_6 and a height h_1, are drilled to enable the assembling the feed-lines.

2.2. Dual-mode Feed Network

The proposed dual-mode feed network shown in Figure 2 consists of two sub- networks, denoted by $P_1 - P_2 - A_1 - A_2$ and $P_3 - P_4 - A_3 - A_4$, respectively. Each sub-network is made of a 3 dB Wilkinson power divider $(P_2 - A_1 - A_2)$ & $(P_4 - A_3 - A_4)$ (blue in Figure 2) and a balun (orange in Figure 2), where the balun in turn is a cascade of a wideband 90° hybrid coupler $(P_1 - L_1 - A_1 - A_2')$ & $(P_3 - L_2 - A_3' - A_4)$ and a quarter-wavelength transmission line $(A_2' - A_2)$ & $(A_3' - A_3)$.

The design of the hybrid coupler is based on the method of [17] and the principle circuit is shown in Figure 2(a). To fit the coupler into the physical space provided by the DPFP feed network, it was mapped into the orange structure shown in Figure 2(b). Using IE3D software, we could optimize the coupler and have achieved a fractional bandwidth of 70%.

As results, the feed network parameters are obtained and shown in Table 2. In Figure 2(b), the right hand half (green) of the feed network is roughly a mirror of the left half. The microstrip dimensions of the feed network are shown in Figure 2(c).

The two sub-networks can be operated at two different modes: Mode 1 and Mode 2. Mode 1 is defined by the anti-phase excited feeding, and is realized by combining a hybrid circuit and a transmission line. Mode 2 is defined by the co-phase excited feeding and is realized by a power divider. The selection of operating mode is accomplished by setting the electrically ON and OFF states using the eight PIN switches D_j ($j = 1, 2, \ldots$ and 8). The electrical states configurations of the PIN switches for the Modes are given in Table 3.

Each pair of the antenna feeding points in the RF circuits $(A_1 - A_2)$

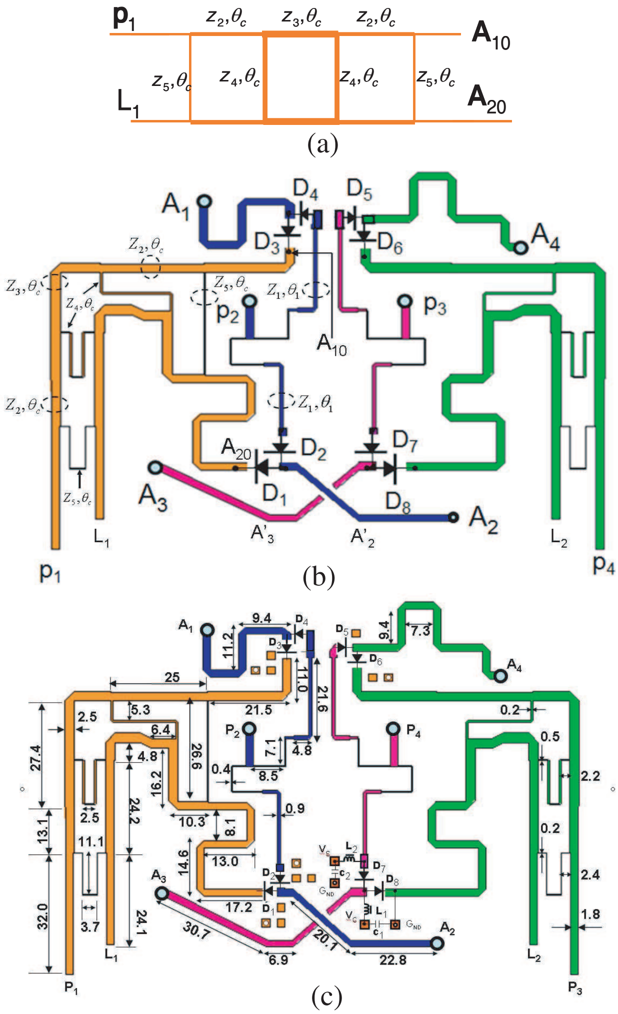

Figure 2. Feed network for the DPFP antenna: (a) principle circuit of the hybrid coupler; (b) physical structure of the feed network circuit; (c) microstrip dimensions of the feed network (unit: mm).

& $(A_3 - A_4)$, is electrically connected with each pair of the T-probe feeders, denoted by $P_{a1} - P_{a2}$ and $P_{a3} - P_{a4}$, through four holes drilled in the antenna bracket. Therefore, $(P_1 - A_1 - A_2)$ & $(P_2 - A_1 - A_2)$ and $(P_3 - A_3 - A_4)$ & $(P_4 - A_3 - A_4)$ are used, with anti-phase and co-phase excitation, respectively, resulting in the orthogonal linear polarizations of the radiated electromagnetic fields.

Table 2. The feed network parameters.

Charac. Impedenc	Z_1	Z_2	Z_3	Z_4	Z_5
Value(Ω)	70.7	45	42	90	139
Elec. Length	θ_1	θ_2	θ_3	θ_4	θ_5
Value(degree)	90	90	90	90	90

Table 3. Electrically states of the eight PIN switches.

	D_1	D_2	D_3	D_4	D_5	D_6	D_7	D_8
Mode 1	ON	OFF	ON	OFF	OFF	ON	OFF	ON
Mode 2	OFF	ON	OFF	ON	ON	OFF	ON	OFF

3. HYBRID BEAMFORMING ALGORITHMS

For the estimation of the direction of arrival it is necessary to collect the radiation pattern for both Mode 1 and Mode 2 simultaneously. To achieve this, the receiver is designed to allow for a time division multiplexing operation: The sample time is defined in consecutive repetitive time slots T_1 and T_2, where T_2 and T_1 are sampling time and $T_2 = T_1 = 0.2083\,\text{ns}$. During the operation, Mode 1 and Mode 2 are turned on and off alternately. For instance, shown in Figure 3, in T_1 the Mode 1 is on and Mode 2 is off, and in T_2 the Mode 1 is off and Mode 2 is on. By doing this we obtain samples for Mode 1 in T_1 and samples for Mode 2 in T_2, repetitively and respectively.

Within the aforementioned time multiplexing reception scheme, the application of DPFP antenna can be enabled in the following three steps:

(1) Construct the sum and difference beam pattern of the received signals in the T_1 and T_2, by using down converted and digitized the received radio signal.

(2) Calculate the first-order radiation pattern $F^{(1)}(\theta)$ in the digital domain by using the sum and difference value.

(3) Compute the second-order radiation pattern $F^{(2)}(\theta)$ by differentiating $F^{(2)}(\theta)$ from the elevation angle θ.

Generally speaking, function $F^{(1)}(\theta)$, as a function of θ, reaches the maximum at the direction of the arrival, i.e., $\theta = 0$. However, due to the complexity of the real propagation environment and the receiver

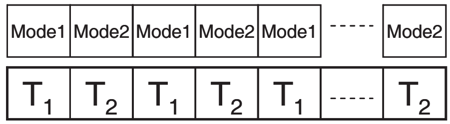

Figure 3. Sample times and corresponding DPFP antenna Mode.

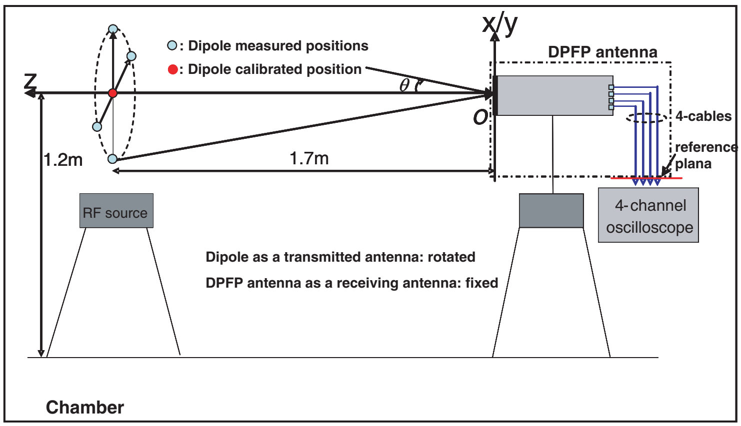

Figure 4. Set up for the calibration and for the beam forming experiment.

system, there exists uncertainty of the angle resolution. To reduce this uncertainty, the second-order radiation pattern $F^{(2)}(\theta)$ is introduced, because the sign of $F^{(2)}(\theta)$ can be used to remove the non-uniqueness of the angle and the absolute value can help determining how close the angle of arrival is to $\theta = 0$.

Before applying the beam forming algorithm, a calibration is necessary for the DPFP antenna ports. As shown in Figure 4, the calibration system consists of a half-wavelength vertical dipole as transmitter located at $(x, y, z) = (0, 0, 1.7\,\mathrm{m})$, which is shown by the red point in Figure 4, a DPFP antenna as receiver located at $(x, y, z) = (0, 0, 0)$, and a four channel oscilloscope connected to the DPFP antenna. The system is installed in a microwave chamber and a continuous sinusoidal wave at frequency 1.25 GHz is transmitted by the dipole antenna.

During the calibrations, the received signals from different ports of the DPFP antenna are measured using the LeCroy 104Xi oscilloscope, The received signals are digitized and transformed, using FFT, into frequency domain, resulting in the channel transfer function denoted by

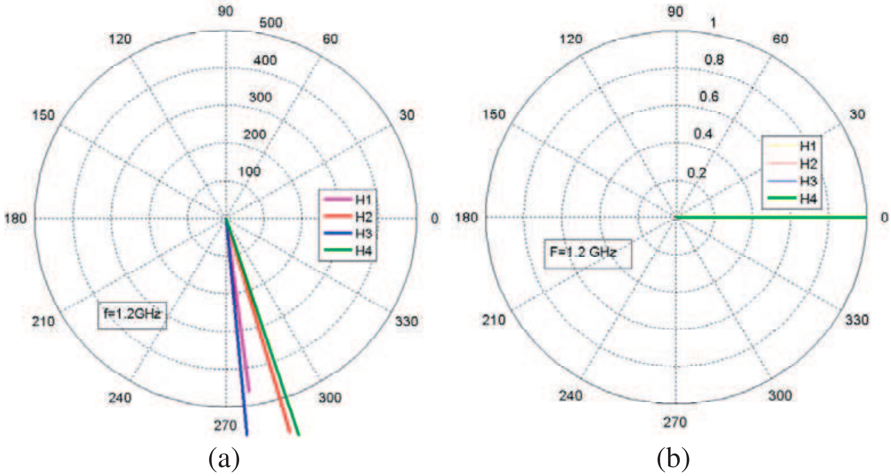

Figure 5. The complex channel transfer function, i.e., H_1, H_2, H_3, H_4. (a) Before the calibration, (b) after calibration.

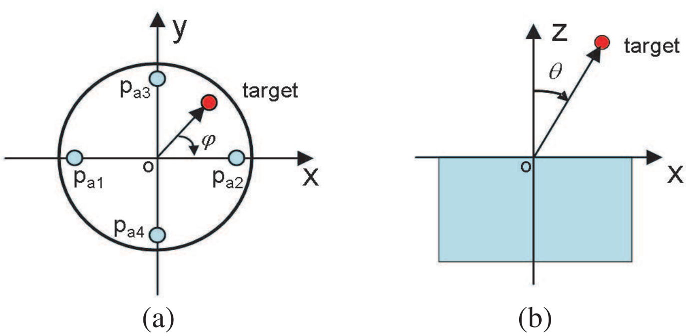

Figure 6. Projections of the reference points defining the channels of DPFP antenna. (a) x-y and (b) x-z planes, respectively.

H_1, H_2, H_3 and H_4, respectively, shown in Figure 5(a). The calibration coefficients for different channels are thus obtained by reciprocal values, i.e., $1/H_1$, $1/H_2$, $1/H_3$ and $1/H_4$, respectively. Later, these coefficients are multiplied to the received signals to remove imbalance in the reception. The channel transfer functions in frequency domain after calibration are plotted in Figure 5(b).

Figure 5(b) shows the transfer functions after the calibration in polar coordination system. It should be pointed out that the channels mentioned here refer to a chain of components: dipole antenna, free propagation path, the DPFP antenna system and the receiver, which are located between the two reference planes, i.e., $z = 1.7\,\text{m}$ and reference plane, in Figure 3. Thus, there are four different channels and each corresponds to a unique port of the DPFP antenna.

3.1. First-order Beam Forming

The electric field $\vec{E}_0\,(\theta, \varphi)$ arrives at the DPFP antenna, as shown in Figure 6, the received signals at Ports A_1, A_2, A_3 and A_4 can be described by

$$V_1 = \vec{E}_0\,(\theta, \varphi) \cdot \vec{G}_1(\theta, \varphi) e^{-jkd \sin\theta \cos\varphi} \tag{1}$$

$$V_2 = \vec{E}_0\,(\theta, \varphi) \cdot \vec{G}_2(\theta, \varphi) e^{jkd \sin\theta \cos\varphi} \tag{2}$$

$$V_3 = \vec{E}_0\,(\theta, \varphi) \cdot \vec{G}_3(\theta, \varphi) e^{jkd \sin\theta \sin\varphi} \tag{3}$$

$$V_4 = \vec{E}_0\,(\theta, \varphi) \cdot \vec{G}_4(\theta, \varphi) e^{-jkd \sin\theta \sin\varphi} \tag{4}$$

where $\vec{G}_i(\theta, \phi)$ ($i = 1, 2, 3$ and 4) is the gain pattern of the calibrated antenna for the electric field at port A_i, while the other antenna ports $P_{a\text{i}}$ are terminated by a $50\,\Omega$ load. In (1)–(4) the parameter d is the distance between P_{a1} and P_{a2} (or P_{a3} and P_{a4}), and k is the wave number. To simplify our analysis, we look at $\varphi = 0°$ and $90°$, and consider the signal sum and difference Σ_{12}, Σ_{34}, Δ_{12} and Δ_{34}, respectively, i.e.,

$$\Sigma_{12}(\theta, \varphi) = (V_1 + V_2) \tag{5}$$

$$\Delta_{12}(\theta, \varphi) = (V_1 - V_2) \tag{6}$$

$$\Sigma_{34}(\theta, \varphi) = (V_3 + V_4) \tag{7}$$

$$\Delta_{34}(\theta, \varphi) = (V_3 - V_4) \tag{8}$$

The first-order radiation pattern $F^{(1)}(\theta)$ is the ratio of anti-phase excited gain pattern to the co-phase excited gain pattern. In specific, for $\varphi = 0°$ (A_1 and A_3) and $\varphi = 90°$ (A_2 and A_4), it is

$$F^{(1)}(\theta) = \left.\frac{|\Delta(\theta, \varphi)|}{|\Sigma(\theta, \varphi)|}\right|_{\varphi=0°,90°} \tag{9}$$

3.2. Second-order Beam Forming

There is still uncertainty in $F^{(1)}(\theta)$ in terms of detection of elevation angle θ angles. To remove the uncertainty, and thus improve the detection reliability, second-order gain pattern $F^{(2)}(\theta)$ which is deployed is defined by

$$F^{(2)}(\theta_n) = \left[F^{(1)}(\theta_n) - F^{(1)}(\theta_{n-1})\right] \tag{10}$$

where $\theta_n = n\pi/180$, $n = 1, 2, \ldots N$, and $F^{(2)}(\theta_n)$ is the nth sampled value of the angle spectrum series, with $\varphi = 0°$ and $\varphi = 90°$.

4. RESULTS AND DISCUSSION

4.1. S-Parameters

Based on the parameters provided by Figures 1 and 3, the proposed DPFP antenna is simulated using the commercial software SEMCAD [18]. Then, a prototype is fabricated and shown in Figure 7. The substrate of feed network and bracket is chosen to be the Taconic RF-60A/PTFE, with the relative permittivity of 6.55/2.55, the loss tangent of 0.0028/0.001, and the height of 1.27/30.0 mm antenna.

The simulated and measured S_{11}-parameter at each T-probe feeder Port A_i ($i = 1, 2, 3$ and 4) without the feed network is plotted in Figure 8. Over the frequency range from 1.01 GHz to 1.79 GHz, the return loss is better than 10 dB.

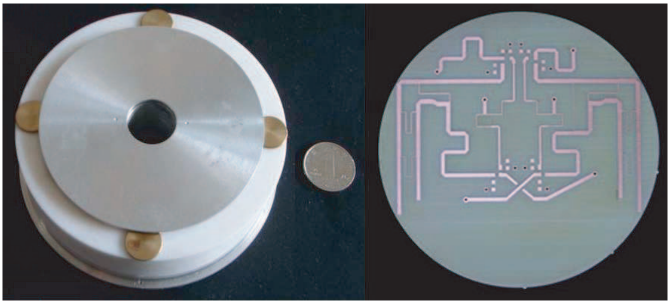

(a) (b)

Figure 7. Fabricated (a) radiation elements and (b) feeding network of the DPFP.

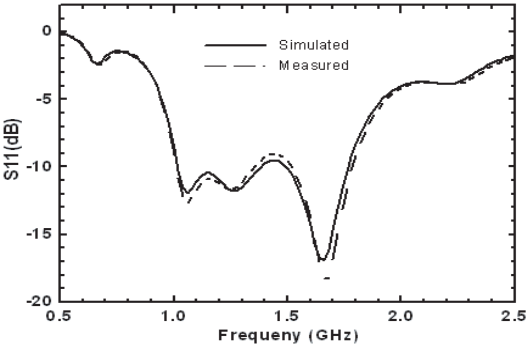

Figure 8. Simulated and measured S_{11}-parameter of the antenna with no feeding network connected.

The deployment of two broadband baluns and two power dividers in the feed network has improved the isolation between the Ports P_1 and P_3 at Mode 1 over the given bandwidth. The transmission line $A_2' - A_2(A_3' - A_3)$ and the position of Port P_2 (or P_4) shown in Figure 2 require careful design to meet the requirements of feed network in both Mode 1 and Mode 2, while Port L_1 (or L_2) is terminated with $50\,\Omega$ load.

Figure 9 shows the simulated return loss and the response of the 180° balun. The relative bandwidth is about 75% when $S_{P1,P1} \leq -10\,\text{dB}$. Also, it is found that the balun can deliver balanced power splitting over the relative bandwidth of 37%, with $S_{A1,p1} = S_{A2,p1} = -3\,\text{dB}$ ($\pm 0.5\,\text{dB}$) and consistent $180°(\pm 5°)$ phase shifting over the band of 1.19–1.81 GHz.

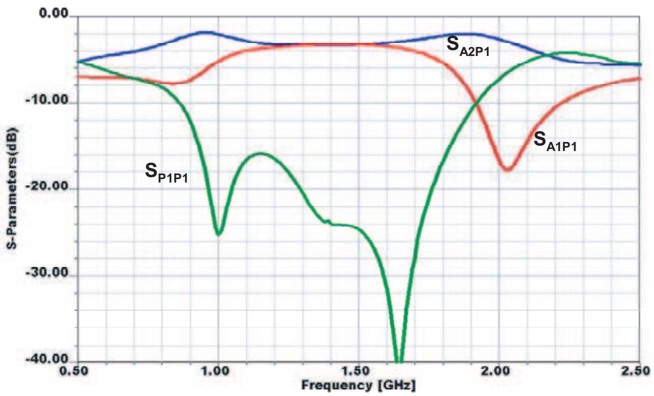

(a)

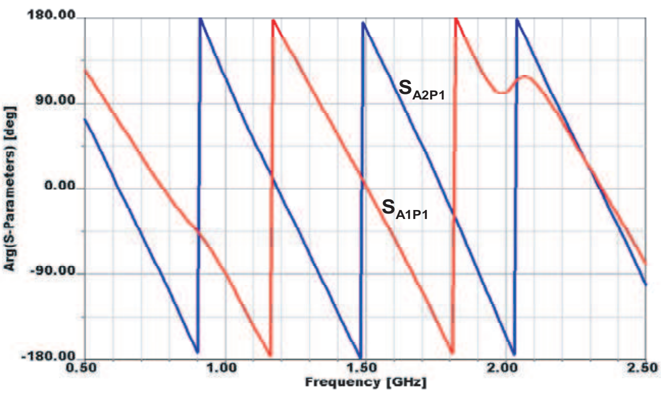

(b)

Figure 9. Simulated S-parameters of the balun as a function of frequency for (a) the magnitude and (b) the phase.

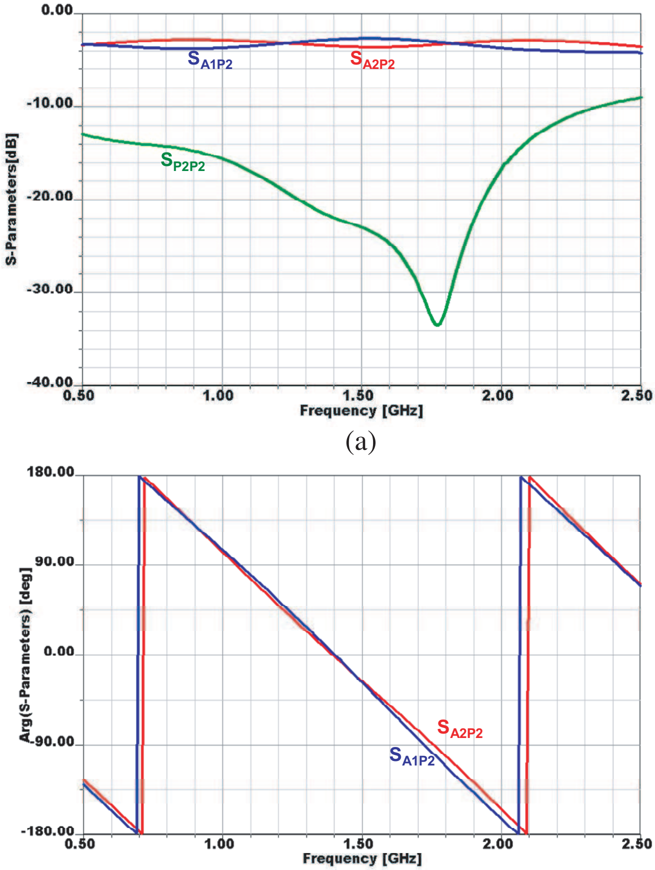

Figure 10. Simulated S-parameters of the power divider as a function of frequency for the (a) magnitude and (b) phase.

Figure 10 shows the simulated return loss and the response of the power divider. The 10 dB return loss bandwidth over 78% is obtained. It is seen that the power divider can deliver balanced power splitting over the relative bandwidth of 55%, with $S_{A1,P2} = S_{A2,P2} = -3\,\text{dB}$ ($\pm 0.5\,\text{dB}$) and consistent $180°(\pm 5°)$ phase shifting over the frequency band of 1.12–1.82 GHz.

The simulated and measured S-parameters of the antenna at Mode 1 are shown in Figure 11(a), with the 10 dB return loss bandwidth of 57% and more than 30 dB isolation over the band of 0.96–1.78 GHz. Figure 11(b) shows the simulated and measured S-parameters of the antenna at Mode 2, where the relative bandwidth is about 37% for $S_{P2,P2} \leq -10\,\text{dB}$.

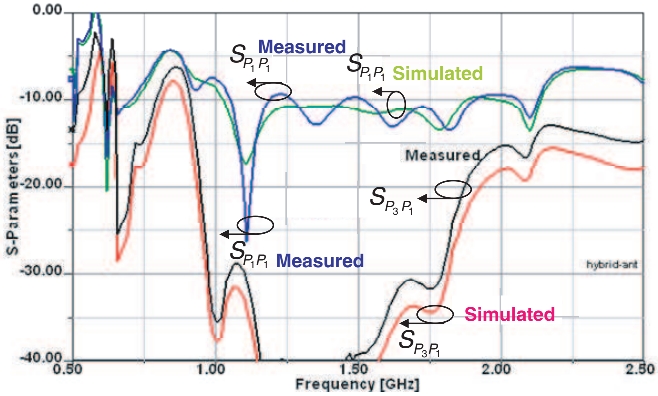

(a)

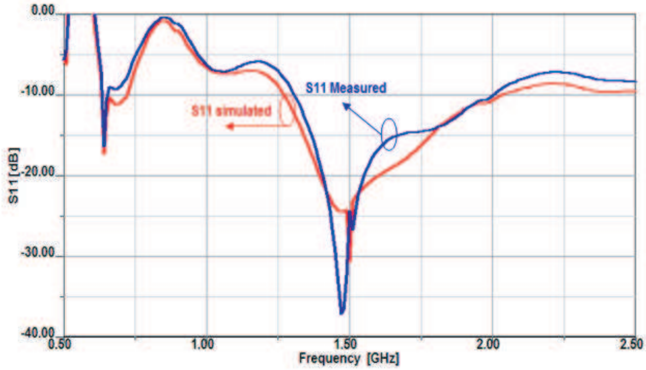

(b)

Figure 11. Simulated and measured S_{11}- and S_{12}- parameters as a function of frequency for the (a) sum and (b) difference beams, respectively.

Two things are important in achieving the expected performance:

(a) The four ports of the radiation element can be seen as port pairs P_{a1}/P_{a2} and P_{a3}/P_{a4}. The distance between ports for each pair is $2r_4$, giving the lower limit of the working bandwidth, while the upper limit of the working bandwidth is given by $2r_{1,}$ the diameter of the radiation patch. (See Figure 1). Correspondingly, r_4 and r_1 are chosen equal to $\lambda_{g1}/2$ and $\lambda_{g2}/2$, where λ_{g1} and λ_{g2} are the guided wavelengths of the lower and higher limit of the working bandwidth, respectively.

(b) The T-probe feeders are vertical to the feed network and the radiation patch, hence their input impedances measured at the feed network and the radiation patch exhibits different values. It is at largest at the top, i.e., P_{a1}. On the other hand there is a capacitive coupling between the edge of the radiation patch and P_{a1}. Therefore, the dimension of the T-probe feeder is chosen so as to provide properly impedance transform from $50\,\Omega$ at the point P_1 to the impedance at the point P_{a1}.

4.2. Radiation Patterns

Figures 12(a) and (b) show the simulated and measured gain patterns of the radiation element at 1.25 GHz and 1.94 GHz, respectively, which are measured at the T-probe feeder Port A_1, with the other T-probe feeder ports (A_2, A_3 and A_4) terminated by the $50\,\Omega$ load, respectively. The single-port feeded antenna has the 3 dB gain beam width of 46° (56°) and the gain of 5.1 dBi (5.0 dBi) at 1.25 GHz (1.94 GHz).

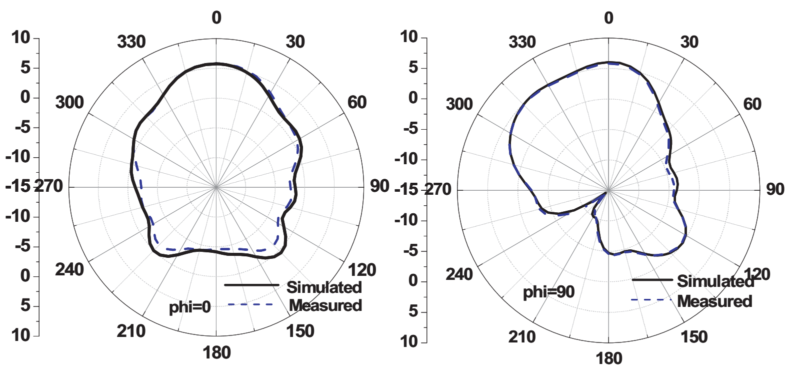

(a)

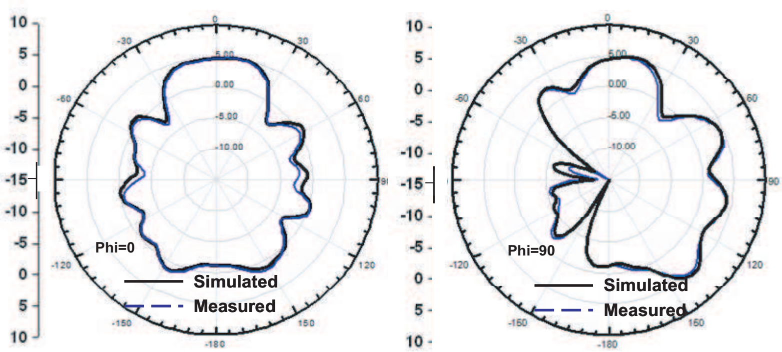

(b)

Figure 12. Simulated and measured radiation patterns of the DPFP antenna. Port A_1 is excited and Ports A_2, A_3 and A_4 are terminated with a $50\,\Omega$ load. (a) $f = 1.25$ GHz and (b) $f = 1.94$ GHz.

The Ports P_1 & P_3 and P_2 & P_4 are symmetrical to each other, resulting in symmetry between A_1 & A_2 and A_3 & A_4. Therefore, only a single polarized radiation pattern of the DPFP antenna is needed to see the performance. This is shown for Modes 1 and 2 in Figure 13. As expected, the radiation pattern is symmetric for both modes, with good agreement between the measurement and simulation. As also indicated by Figure 9, the DPFP antenna possesses a resonant point at 1.6 GHz, when the half-wave length, i.e., 93.7 mm is within the vicinity of the main patch's diameter (92.2 mm).

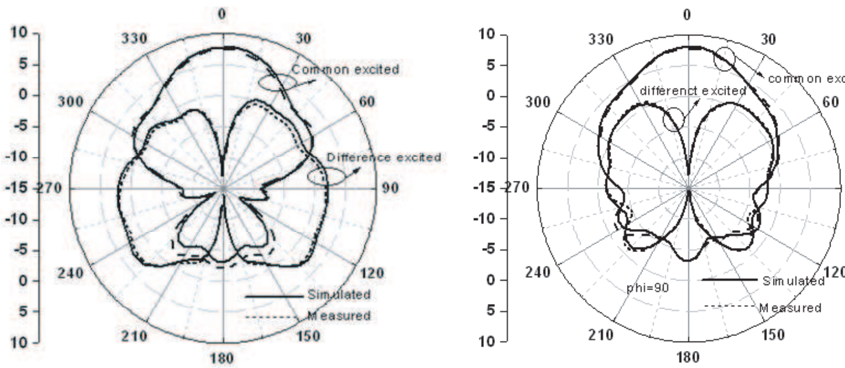

(a) (b)

Figure 13. Simulated and measured radiation patterns of the DPFP antenna, with the Ports P_1 or P_3 excited and Ports P_2 and P_4 terminated with the $50\,\Omega$ load, respectively. (a) $\varphi = 0°$ and (b) $\varphi = 90°$.

As Figure 13 indicates, the antenna behaves like two connected one-quarter wavelength planar inverted F antennas for the co-phase excitation (Mode 1) with anti-symmetrical current distribution. For anti-phase excitation (Mode 2), the antenna behaves like two connected one-quarter wavelength planar inverted F ones, with symmetrical current distribution.

The first-order radiation patterns of the DPFP antenna at 1.25 GHz are plotted in Figure 14, when Ports P_1 and P_3 are excited while Ports P_2 and P_4 are being terminated by the $50\,\Omega$ load. Although the figure only shows three types of radiation patterns of single and double excited modes, it is easy to conclude that by an adequate excitation of these four ports, any two-dimensional radiation pattern, depending on θ and φ, can be obtained.

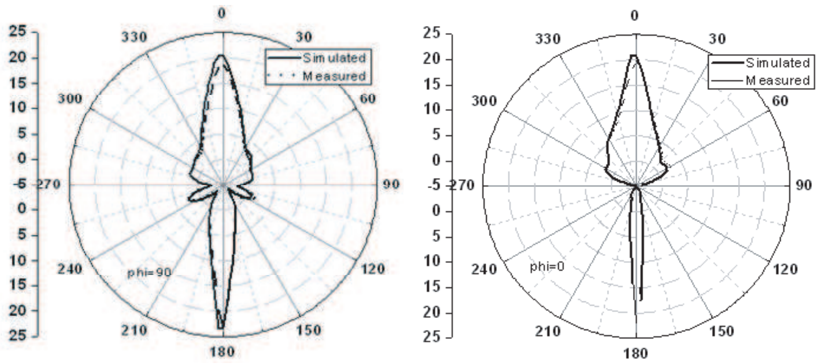

(a) (b)

Figure 14. The first-order radiation pattern $F_{\varphi}(\theta)$ (baseband) of the DPFP antenna. (a) $\varphi = 0°$ and (b) $\varphi = 90°$.

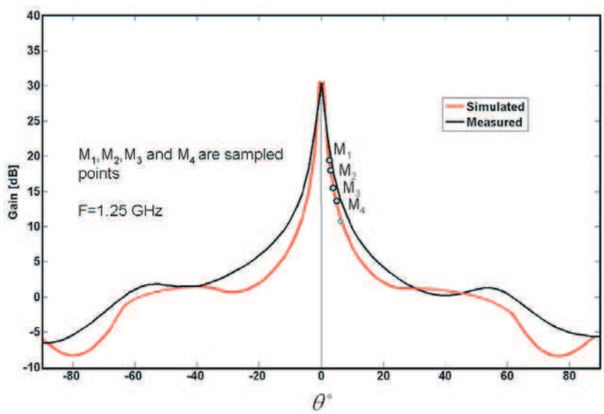

Figure 15. The first-order channel gain $F^{(1)}(\theta)$ of P_1/P_2 pair, for $\varphi = 0°$ (Base band).

4.3. Validation by Measurement

For the measurement, the transmitting dipole antenna is put into the reference coordinate system, where the DPFD antenna is located at the origin, with $z = 1.7\,\text{m}$ and $\theta = 0°$. Then, the dipole antenna is moved along a circle centered at $(x, y, z) = (0, 0, 1.7\,\text{m})$. Thus, the trajectory of the measurement points and the DPFP aperture center make together a cone with apex at the aperture center and measurement points on the perimeter. By changing the radius of the perimeter, values of different theta can be obtained. The results from measurement and simulation are shown in Figure 15.

Table 4. Reference and estimated angles.

	Ref. Level(dB)	Measured Level(dB)	Ref. Angle(deg)	Measured Angle(deg)
M_1	19.4	16.6	0.0	2.0
M_2	14.8	12.4	2.0	3.2
M_3	16.9	12.1	4.0	5.0
M_4	15.1	10.8	6.0	7.0

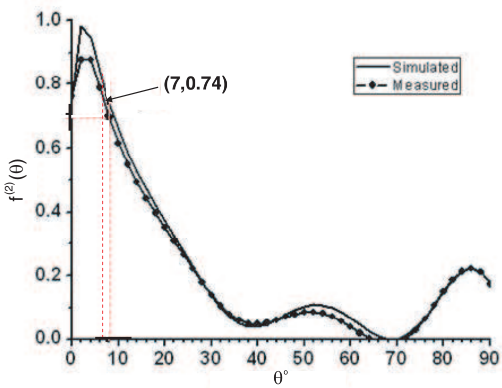

Figure 16. The second-order channel gain of the DPFP antenna when $\varphi = 0°$ (base band).

To visualize the accuracy, four sampled points, i.e., M_1, M_2, M_3 and M_4, are chosen, to compare with the corresponding simulated values. As shown in Table 4, the difference between the simulated and the measured data is within 3°.

For the tracking measured we have deployed the second-order beam forming algorithm. As mentioned in Section 3.1, the second-order beam pattern $F^{(2)}(\theta)$ is the derivation of the first-order beam pattern $F^{(1)}(\theta)$, with respect to theta. Figure 16 shows the $F^{(2)}(\theta)$ computed from the simulated and measured $F^{(1)}(\theta)$, respectively.

5. CONCLUSION

We have presented a compact broadband four-port DPFP antenna, in which we designed the antenna structure, measured the parameters and validated a beam forming algorithm. The miniaturized antenna is 150.0 mm in diameter and 47.0 mm in height, and is capable of operating over the frequency range of 1.0–1.8 GHz, with $S_{11} < -10\,\text{dB}$

and 5.5 dBi single port gain. It is found that 10 dB return loss bandwidth is over 57% and more than 30 dB isolation is over the band of 0.96–1.78 GHz for single as well as dual polarized operations when the radiation element integrated with the feed network. A system level test bed is designed for the validation. Using the test bed, the implemented beam forming algorithm is validated using a fabricated DPFP antenna sample. A good agreement between the simulated and measured results is achieved. The system level experiment confirms that its angular detection accuracy of 7° can be achieved. With this performance, we believe that the DPFP antenna can be used for many wireless communications applications.

ACKNOWLEDGMENT

This work was supported by the National Science Fundation for Creative Research Groups under Grant of 60821062 of China, by the National Basic Research Program under Grant of 2009CB320204 of China and by Major National S&T Program under Grant of 2011ZX03001-003-02 of China.

REFERENCES

1. Fontana, R. J., E. A. Richley, A. J. Marzullo, et al., "An ultra wideband radar for micro air vehicle applications," *2002 IEEE Conference on Ultra Wideband Systems and Technologies*, 187–191, Baltimore, MD, May 2002.
2. Nakano, H., R. Satake, and J. Yamauchi, "Extremely low-profile, single-arm, wideband spiral antenna radiating a circularly polarized wave," *IEEE Trans. Antennas Propag.*, Vol. 58, No. 5, 1511–1520, May 2010.
3. Montero, R. S., S. S. Sanz, J. A. Figueras, and R. Langley, "Hybrid PIFA-patch antenna optimized by evolutionary programming," *Progress In Electromagnetics Research*, Vol. 108, 221–234, 2010.
4. Guo, Y. X., K. M. Luk, and K. F. Lee, "L-probe fed thick substrate patch antenna mounted on a finite ground plane," *IEEE Trans. Antennas Propag.*, Vol. 51, No. 8, 1955–1963, Oct. 2003.
5. Islam, M. T., M. N. Shakib, and N. Misran, "Design analysis of high gain wideband L-probe FED microstrip patch antenna," *Progress In Electromagnetics Research*, Vol. 95, 397–407, 2009.
6. Krairiksh, M., P. Keowsawat, C. Phongcharoenpanich, and S. Kosulvit, "Two-probe excited circular ring antenna," *Progress In Electromagnetics Research*, Vol. 97, 417–431, 2009.

7. Secmen, M. and A. Hizal, "A dual-polarized wide-band patch antenna for indoor mobile communication applications," *Progress In Electromagnetics Research*, Vol. 100, 189–200, 2010.
8. Liang, G., W. B. Gong, H. J. Liu, and J. P. Yu, "Development of 61-channel digital beamforming transmitter array for mobile satellite communication," *Progress In Electromagnetics Research*, Vol. 97, 177–195, 2009.
9. Huang, Y. and P. V. Brennan, "FMCW based MIMO imaging radar for maritime navigation," *Progress In Electromagnetics Research*, Vol. 115, 327–342, 2011.
10. Mallahzadeh, R., S. Eshaghi, and A. Alipour, "Design of an E-shaped MIMO antenna using IWO algorithm for wireless application at 5.8 GHz," *Progress In Electromagnetics Research*, Vol. 90, 187–203, 2009.
11. Byrne, D., M. O'Halloran, M. Glavin, and E. Jones, "Data independent radar beamforming algorithms for breast cancer detection," *Progress In Electromagnetics Research*, Vol. 107, 331–348, 2010.
12. Kingsley, S. P. and S. G. O'Keefe, "Steerable-beam multiple-feed dielectric resonator antenna," U.S. Patent 6,900,764 B2, May 31, 2005.
13. Chiu, C. Y. and R. D. Murch, "Compact four-port antenna suitable for portable MIMO devices," *IEEE Antennas Wireless Propag. Lett.*, Vol. 7, 142–144, 2008.
14. Yin, J., D. Nyberg, X. M. Chen, and P. S. Kildal, "Characterization of multi-port eleven antenna for use in MIMO system," *IEEE International Symposium on Wireless Communication Systems, (ISWCS'08)*, 2008.
15. Yin, J., J. A. A. J. Yang, and P. S. Kildal, "Monopulse tracking performance of multi-port eleven antenna for use in satellite communications terminals," *Proceedings of 2nd European Conference on Antennas and Propagation*, Nov. 2007.
16. Wu, B. and K. M. Luk, "A 4-port diversity antenna with high isolation for mobile communications," *IEEE Trans. Antennas Propag.*, Vol. 59, No. 5, 1660–1667, May 2011.
17. Muraguchi, M., T. Yukitake, and Y. Naito, "Optimum design of 3-dB branch-line couplers using microstrip lines," *IEEE Trans. Microw. Theory Tech.*, Vol. 31, No. 8, 674–678, Aug. 1983.
18. Schmid & Partner Engineering AG, SEMCAD-X manual.pdf, May 2009.